

Modification of the Solid Electrolyte Interphase on SiGr Electrodes by a Prelithiation Method Using Passivated Lithium Metal Powder

Ekin Esen, Iratxe de Meatz, Martin Schmuck, Mohsen Padervand, Martin Winter, Elie Paillard,* and Masoud Baghernejad*

Negative electrode materials with high specific energy, such as SiGr, are essential to decrease battery cell weight and volume while allowing improved range and design flexibilities for electric vehicles. Among different SiGr anode prelithiation methods, the use of passivated lithium metal powder is discussed in terms of cell impedance and its effects on the interphase film formation on SiGr and $\text{LiNi}_{0.8}\text{Mn}_{0.1}\text{Co}_{0.1}\text{O}_2$ (NMC-811) electrodes with high mass loadings. Electrochemical impedance spectroscopy analyses show that a less resistive and more effective solid electrolyte interphase (SEI) forms upon prelithiation which also benefits the charge transfer at the SiGr electrode. Scanning electron

microscopy images show a thicker interphase layer with less interstitial porosity on the prelithiated SiGr electrodes and a thinner cathode electrolyte interphase on NMC-811 electrode as a result of the lower average cathode potential attained throughout cycling, in comparison with the cells without prelithiation. A more diverse SEI layer, richer in beneficial components such as LiF, is promoted by the prelithiation method as shown by X-ray photoelectron spectroscopy with a sputtering depth of 100 nm. Finally, it is shown that the more robust SEI layer forming upon prelithiation requires less electrolyte consumption for repairing the SEI layer throughout long-term cycling.

1. Introduction

In addition to their supremacy in the consumer electronics market for the past three decades, lithium-ion batteries have also

become dominant in the emerging electric vehicle (EV) market.^[1] Demands of the EV market have increased the expectations on battery performance to be able to compete with the combustion engines, which requires improvement of the energy density at battery pack and cell levels.^[2] Therefore, materials with high specific capacity such as silicon (Si) negative electrodes (3579 mAh g^{-1} _{Si})^[3] and nickel-rich positive electrodes ($>200 \text{ mAh g}^{-1}$ _{NMC-811} at 4.2 V)^[4] have attracted the interest of battery researchers for their superiority over the state-of-the-art graphite (372 mAh g^{-1} _{Gr}) and NMC111 ($150\text{--}170 \text{ g}^{-1}$ _{NMC-111}) electrodes. Despite their advantages, these materials bring substantial challenges regarding the performance and lifetime. A major drawback of Si electrodes is the large volume change of Si as a result of formation of intermetallic phases (=simply called alloying and dealloying) with lithium (Li) during lithiation and delithiation of the electrode which can reach up to 300% of its initial volume.^[5] If the formed solid electrolyte interphase (SEI) is not effective, this volume change causes poor Coulombic efficiency (CE) throughout cycling as the continuously broken and rebuilt SEI consumes active lithium and the electrolyte.^[6] Moreover, it causes poor cycling stability as Si particles degrade and pulverize and eventually become electrically isolated from the electrode bulk, leading to rapid capacity losses.^[7,8] It is known that, for lithium storage hosts such as Si, reducing the particle size limits crack formation during galvanostatic cycling due to lower mechanical strain during the alloying and dealloying processes. However, the resulting high surface area increases active lithium consumption during SEI formation, resulting in reduced initial Coulombic efficiency (ICE), typically ranging between 25% and 75%.^[9] Replacing pure Si electrodes with SiGr core–shells structures^[10] or silicon carbon (SiGr) composites mixed with

E. Esen, M. Winter, M. Baghernejad
Helmholtz-Institute Münster, IMD-4, Forschungszentrum Jülich GmbH
Corrensstraße 46, 48149 Münster, Germany
E-mail: b.masoud@fz-juelich.de

E. Esen, I. de Meatz
CIDETEC, Basque Research and Technology Alliance (BRTA)
CIDETEC, Po. Miramón 196, 20014 Donostia-San Sebastian, Spain

M. Schmuck
VARTA Innovation GmbH
Am Innovationspark 10, Graz 8020, Austria

M. Padervand
Department of Chemistry
Faculty of Science
University of Maragheh
P.O Box 55181-83111, Maragheh, Iran

M. Winter
Münster Electrochemical Energy Technology
Corrensstraße 46, 48149 Münster, Germany

E. Paillard
Department of Energy
Politecnico di Milano
Via Lambruschini 4, 20156 Milan, Italy
E-mail: elielisee.paillard@polimi.it

 Supporting information for this article is available on the WWW under <https://doi.org/10.1002/batt.202500514>

 © 2025 The Author(s). *Batteries & Supercaps* published by Wiley-VCH GmbH. This is an open access article under the terms of the Creative Commons Attribution License, which permits use, distribution and reproduction in any medium, provided the original work is properly cited.

graphite (Gr)^[11–13] can help limit the disadvantages associated with volume change while still offering higher specific capacity compared to the state-of-the-art graphite electrodes. However, neither of these approaches fully addresses the loss of active Li required for formation and continuous repair of the SEI, nor do they ensure stable, long-term galvanostatic cycling with high CE.

Prelithiation of the negative electrodes is an effective technique to provide additional lithium to the cells to compensate the losses of active lithium related to the SEI formation and improving the ICE. Prelithiation can be performed electrochemically by partially charging the negative electrode in a separate cell,^[6] chemically using sacrificial Li-containing reagents,^[14–16] or through direct contact of the electrode with passivated lithium metal powder (PLMP)^[17,18] or Li foil.^[19,20] Although precise control over the prelithiation degree is achievable with each of these methods, they all have inherent drawbacks. In addition to increased cost, using sacrificial lithium compounds requires an additional degassing step after the formation cycles which increases the process time.^[21] Similarly, prelithiating the electrodes electrochemically requires the disassembly of the half-cells used for prelithiation and the reassembly of a new cell with the prelithiated electrode, leading to increased process time and cost.^[6] Compared to these methods, prelithiation by direct contact with lithium metal or powder is more convenient as it does not require degassing or cell reassembly. However, the process needs to be completed in a dry room or in a glove box.^[22] As reported in our previous publication, an intriguing outcome of the direct contact method is that the sudden potential decrease of the SiGr electrode upon contact with Li as well as the reactive Li remaining on the electrode surface allows the simultaneous reduction of all the electrolyte components, leading to a different SEI composition compared to electrochemically prelithiated electrodes.^[23] Thus, this method has the potential to affect and improve the SEI properties while compensating for the ICE losses.

Methods to modify SEI layer on various anodes have been widely reported in the literature. Wellmann et al. reported a mechanochemical method using ionic liquids to form an artificial SEI layer on Li metal electrodes,^[24] while 1-pentylamine^[25] or fluoroethylene carbonate (FEC) and vinylene carbonate (VC) were also used for Li metal electrodes.^[26] Zhao et al. have investigated Li_xSi nanoparticles as both an anode material and a prelithiation agent for Si, Sn, and Ge electrodes.^[27] Augustine et al. used Li_{1.3}Al_{0.3}Ti_{1.7}(PO₄)₃ (LATP) coating to form an artificial SEI on Si particles which also acted as a Li reservoir.^[28] Moreover, Li₃P that is also used as a cathodic prelithiation agent for Li-ion batteries,^[29] was proposed as an artificial SEI to improve the galvanostatic cycling stability of the Si electrodes.^[30] Similarly, lithium phosphorous oxynitride (LiCPON/LiPON) that was also reported as a prelithiation agent for the SiO_x-C electrodes,^[31] was proposed to form an artificial SEI on Si thin film anodes.^[32] When PLMP is used as a prelithiation reagent, passive lithium powder is added on the electrode surface, and its interphase shell (Li₂CO₃) is broken by applying pressure to ensure the contact of lithium and anode material (Figure 1). When lithium is pressed on the SiGr electrodes for prelithiation, parts of the electrode surface behave similar to a Li metal electrode while the reduction of the electrolyte also

occurs on lithiated Si and Gr particles. Therefore, individual studies conducted on Li metal, Gr, or Si surfaces regarding how the SEI is formed on these electrodes are insufficient to fully understand the SEI formation on the SiGr electrodes prelithiated using PLMP. Thus, addressing this gap is necessary to enable better tailoring of the interfacial films for similar systems. We have previously reported that the cycle life of NMC-811 (21.0 mg cm⁻²) || SiGr (6.6 mg cm⁻²) cells can be tripled by adjusting the prelithiation conditions, such as storage time, as this drastically affects the cell impedance.^[23] We have also shown that, after long-term galvanostatic cycling, prelithiation using PLMP promotes an SEI layer richer in inorganic components. Here, a complementary study using electrochemical impedance spectroscopy (EIS) analyses is reported to show how prelithiation using PLMP dramatically decreases the total cell impedance during the initial cycles by promoting a superior SEI. A comprehensive postmortem analysis of NMC-811 || SiGr lithium-ion cells, including extensive X-ray photoelectron spectroscopy (XPS) analyses, performed on both prelithiated and nonprelithiated SiGr electrodes as well as on the NMC-811 electrodes highlights the composition differences of the SEI on SiGr and NMC-811 electrodes after formation cycles and after 300 cycles.

2. Results and Discussion

2.1. Impedance Evolution during the Formation Cycles

EIS measurements were performed for the NMC-811 || SiGr coin cells consisting of prelithiated (2.5 wt% Li) or nonprelithiated SiGr electrodes to observe the impedance change during the formation cycles (1x C/10, 3x C/3) as well as for the six subsequent cycles at C/3. The equivalent circuit used was $Z = R_b + R_{SEI/CEI}\text{-CPE}_{SEI/CEI} + R_{ic}\text{-CPE}_{ic} + R_{ch-tr}\text{-CPE}_{ch-tr} + W$ (Figure 2a)^[11] and the Nyquist plots for each charge and discharge step are shown in Figure 2b–e. As can be seen, the total cell impedance increases for both prelithiated and nonprelithiated cells as cycling proceeds, although the increase is more prominent for the nonprelithiated cell. It is worth noting that the three semicircles can be seen for all cells after the charge steps, but they overlap after the discharge steps, making it harder to estimate the contribution of each circuit component. Each spectrum was fitted according to the same equivalent circuit, and the fitting data are presented in Figure 3 to elucidate the individual contribution of each resistance component.

The high-frequency region of the EIS spectra shows the R_b value, which provides information on the state-of-health of a battery cell, as it is affected by factors such as crack formation in particles, depletion of electrolyte, binder decomposition, current collector dissolution, and gas evolution in the Li-ion cells.^[33] Besides crack formation, these parameters are not affected by the state-of-charge (SoC) of the cells, hence the R_b value is rather independent of the SoC.^[33] The measured R_b values varied between 6.0 and 10.0 Ω cm² for both prelithiated and nonprelithiated cells during the first ten cycles while a slightly higher average R_b value was measured for the prelithiated cell (9 Ω cm²)

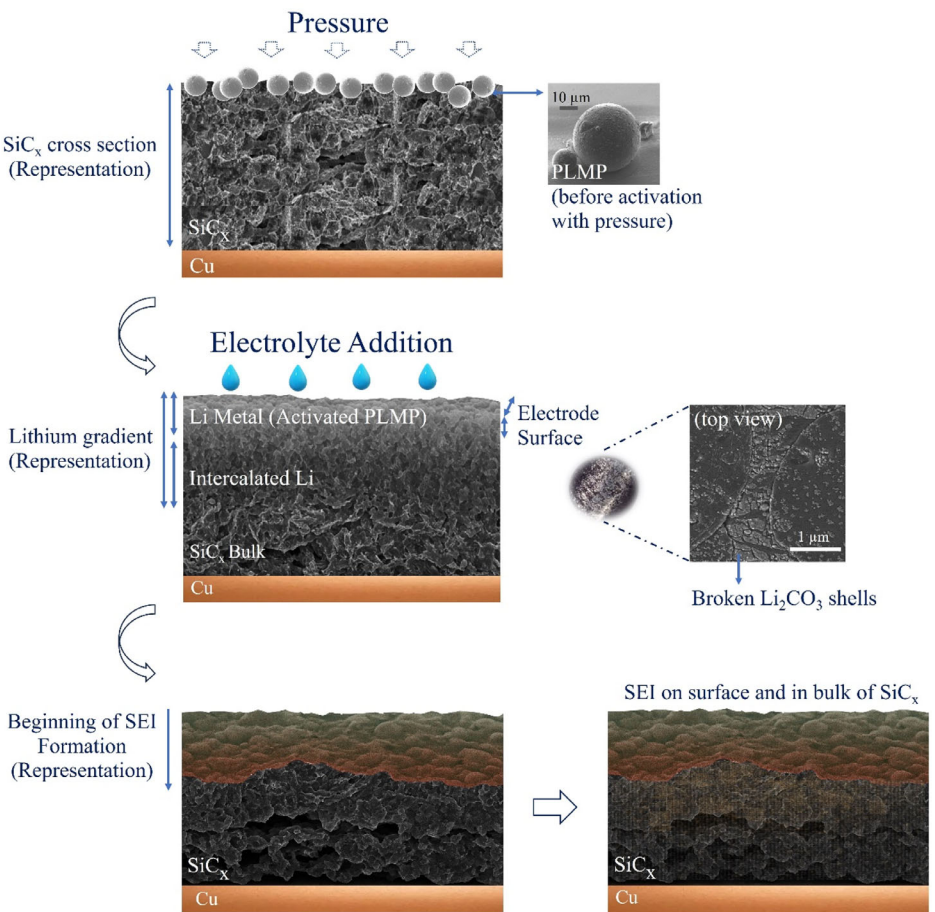


Figure 1. Scheme showing SEI formation upon applying passivated lithium metal powder on the negative electrode surface for prelithiating the electrode prior to galvanostatic cycling. Note: This image is generated by ChatGPT on 27.05.2025, utilizing the SEM images produced for the work. Images are representations and proportions are exaggerated for clearer expression.

compared to the nonprelithiated one ($\approx 7 \Omega \text{ cm}^2$) during the first cycle (Figure 3). We assume that this observation is attributed to the electrolyte consumption for SEI formation upon lithiation of the SiGr electrodes since this occurs in the prelithiated cells prior to cycling.^[23,33,34] R_b values measured after each charge and discharge steps were almost equal ($\approx 8.0 \Omega \text{ cm}^2$) for the prelithiated cells. However, for the nonprelithiated cells slightly lower R_b values were measured after the charge steps ($\approx 6.5 \Omega \text{ cm}^2$) compared to the discharge steps ($\approx 8.5 \Omega \text{ cm}^2$). Among the parameters that affect bulk resistance, crack formation can be expected to change with the lithiation degree of the SiGr electrode in addition to electrolyte depletion as reactions forming the SEI layer continuously occur on the electrode surface.^[33] Thus, in the nonprelithiated cell, the small difference in R_b values between charge and discharge steps hints to a relatively stronger effect on bulk resistance, possibly related to electrolyte depletion.

The first semicircle in the high-frequency region corresponds to $R_{\text{SEI}/\text{CEI}}$ whereas the second and third semicircles at lower frequency region correspond to R_{ic} and $R_{\text{ch-tr}}$.^[11,35] The resistances related to the interphase layers $R_{\text{SEI}/\text{CEI}}$ were similar for both prelithiated and nonprelithiated cells after the first charge and discharge steps. $R_{\text{SEI}/\text{CEI}}$ stayed rather constant during the first six

cycles for the prelithiated cells despite a slight increase after the third cycle, which indicates a rather stable interphase film on the prelithiated SiGr electrodes. Starting from the seventh cycle, $R_{\text{SEI}/\text{CEI}}$ becomes relatively less stable while still staying in the $3\text{--}6 \Omega \text{ cm}^2$ interval until the end of the measurement (ten cycles). On the other hand, changes in $R_{\text{SEI}/\text{CEI}}$ showed a different trend for the nonprelithiated cells especially after the charge steps. When the C-rate of charge increases to C/3, in the second cycle, a rapid increase in $R_{\text{SEI}/\text{CEI}}$ is observed for the nonprelithiated cells. The $R_{\text{SEI}/\text{CEI}}$ value measured for the nonprelithiated cells was roughly 10 times ($10.7 \Omega \text{ cm}^2$) that of the prelithiated cells ($1.1 \Omega \text{ cm}^2$). An irregularity in $R_{\text{SEI}/\text{CEI}}$ values was notable after the sixth charge step for both nonprelithiated and prelithiated cells. The impedance related to interphase layers measured after the charge step reached $2.4\text{--}4.6 \Omega \text{ cm}^2$ for the prelithiated cells while this value was higher for the nonprelithiated cells by a factor of 3–5 difference ($11.7\text{--}13.7 \Omega \text{ cm}^2$) and larger standard deviations. These EIS results demonstrate that, in addition to being more stable, the interphase formed in the prelithiated cells is less resistive compared to those of the nonprelithiated cells. A similar result was reported by Tokranov et al. as they compared the SEI films on Si electrodes that formed during the first cycle by “slow

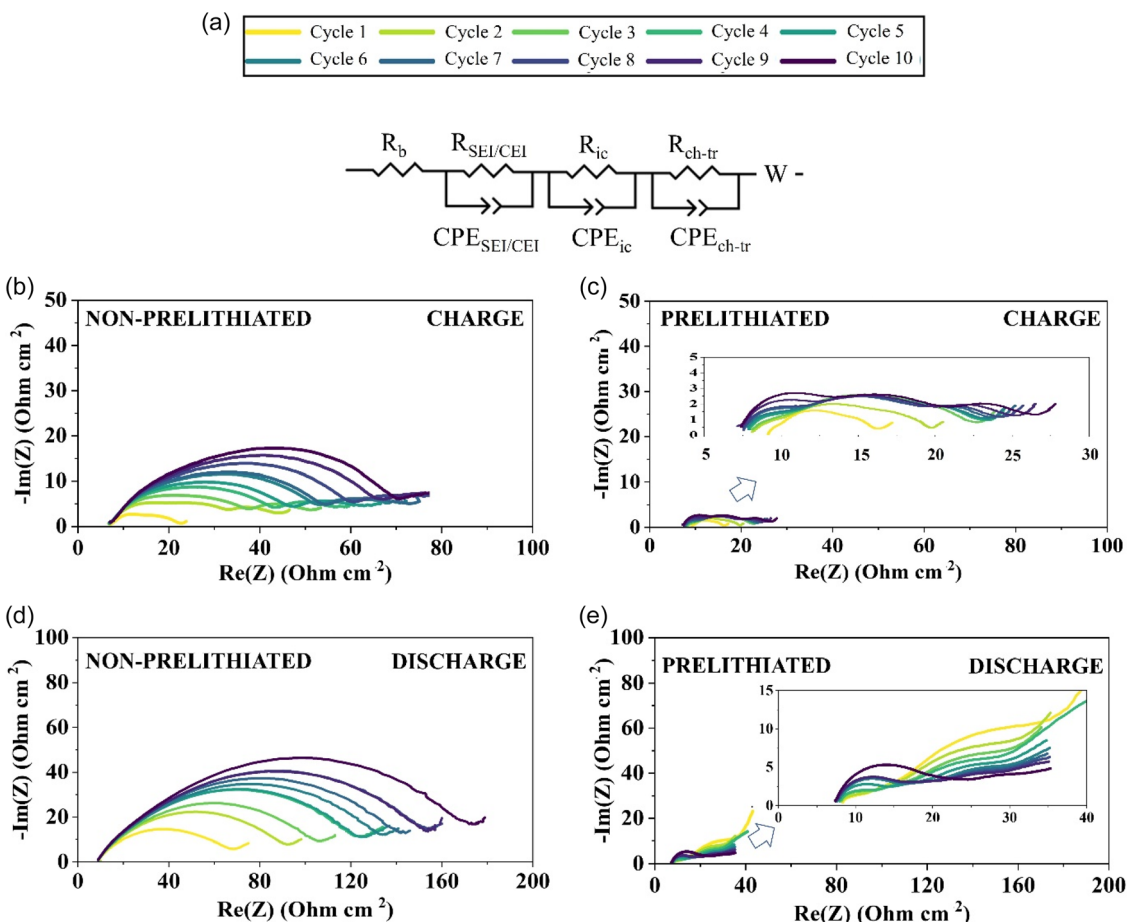


Figure 2. a) Equivalent circuit used to define the NMC-811 || SiGr cells. Nyquist plots showing impedance of the fully charged NMC-811 || SiGr cells during the first 10 cycles for b) nonprelithiated cell and c) prelithiated cell after as well as for fully discharged d) nonprelithiated cell and e) prelithiated cell. (CCCV charge up to 4.2 V and CC discharge down to 2.8 V).

cycling” (0.3–1.2 V) and “pulse cycling” (≤ 0.3 V) and concluded that the SEI layer formed at lower electrode potentials (similar to prelithiated SiGr electrode) was thinner and considerably less resistive.^[36] Such an ample difference in $R_{SEI/CEI}$ must be due to differences in film thicknesses as well as the differences in SEI/CEI compositions which are further discussed in the following sections.

The second semicircle is defined as the interface electronic contact resistance (R_{ic}) that arises due to the insufficient electronic contact between current collectors and the electrode constituents (active material/conductive additive(s)/binder).^[11,37] Pritzl et al. reported that the release of protic species (e.g., HF) upon degradation of LiPF₆ containing electrolytes, leading to the formation of a resistive and insoluble layer (e.g., AlF₃) on the Al current collector while also degrading the Si surface is a major reason for an increase in R_{ic} .^[12,38,39] As can be seen in Figure 3b,d, prelithiation leads to much lower R_{ic} values compared to the nonprelithiated cells. This can simply be explained by lower stress related to volume changes and thus better contact as well as the lack of H₂O that is present in most electrolytes. As extensively reported, HF forms in LiPF₆ containing electrolytes as a reaction product of H₂O and PF₅.^[12,40,41] For prelithiated cells, the electrolyte was

added on the electrode surface that was covered by the PLMP. After activation, the PLMP is very reactive toward H₂O, thus the trace amount of H₂O in the cell is likely consumed before cycling the cells, thereby limiting HF formation during cycling.

The third semicircle in the mid frequency region shows R_{ch-tr} that is a major contributor to the total cell impedance.^[33] The large volume changes of Si particles during cycling are reported to increase R_{ch-tr} as it causes uneven strain-stress distribution in electrodes, leading to electrical isolation of active materials as cycling proceeds.^[11,42] R_{ch-tr} is the major contributor to the total cell impedance for the nonprelithiated cell and it continuously and dramatically increases during the first ten cycles whereas the R_{ch-tr} values measured after the charge steps are 2–3 times lower for the prelithiated cells and become rather stable after the second cycle. The difference in R_{ch-tr} values measured after the discharge steps (delithiation of the SiGr electrodes) was larger compared to the charge steps, reaching up to 13 times those of the prelithiated cell at the eighth cycle. This major difference can be explained by two reasons. First, the SEI formation on prelithiated SiGr electrodes shows different characteristics from the nonprelithiated cells as electrolyte components are reduced simultaneously on the electrode surface, rather than

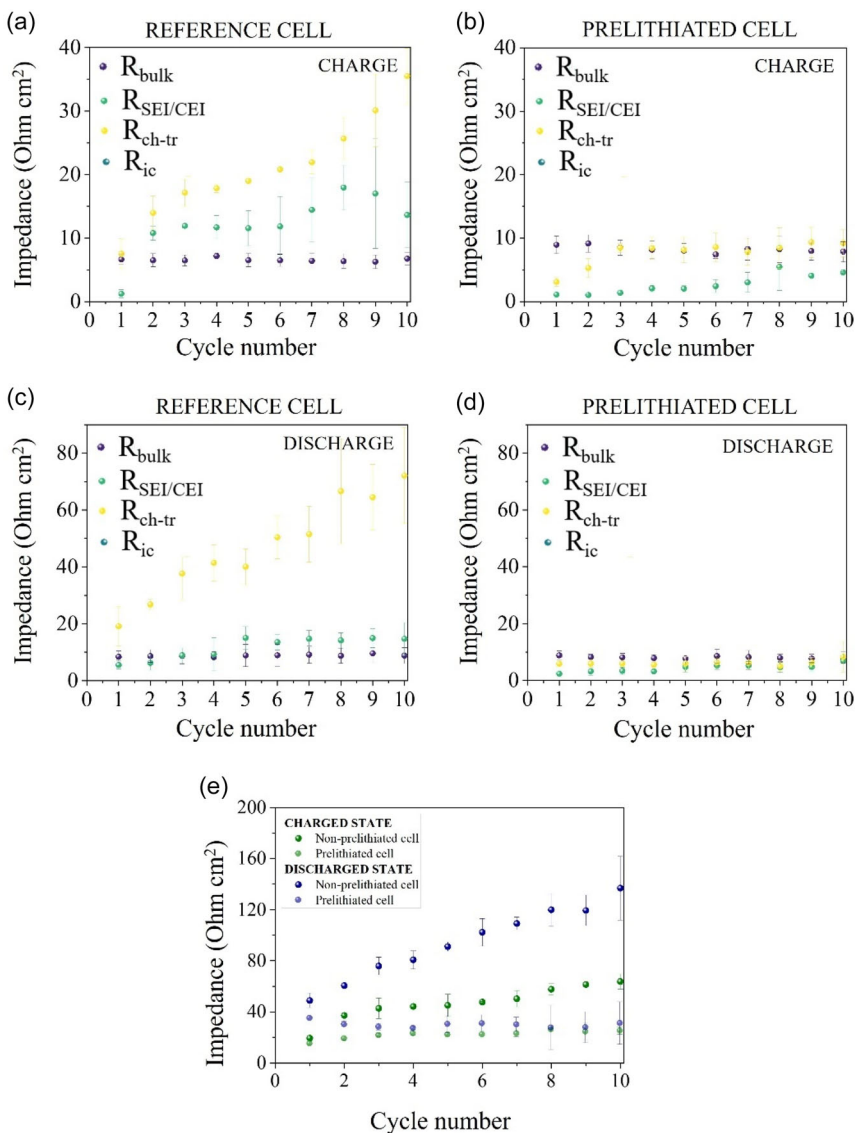


Figure 3. Changes of R_b , $R_{SEI/CEI}$, R_{ic} , and R_{ch-tr} during the first ten cycles. a) Nonprelithiated cell at charged state, b) prelithiated cell at charged state, c) nonprelithiated cell at discharged state, d) prelithiated cell at discharged state, and e) change of total cell impedance during the initial ten cycles at charge and discharged states. The three Nyquist plots showing the highest consistency out of four repetitions were selected for the calculations.

the successive reduction of each component, as soon as the electrolyte is added on the electrode surface covered by lithium powder prior to cycling.^[23] Thus, it is likely that a more ionically conductive SEI is formed on the prelithiated SiGr electrode. Second, as explained in our previous publication, the precycling lithiation of a prelithiated SiGr electrode takes ≈ 7 days^[23] whereas it happens in less than 12 h for the nonprelithiated cells during the first charge step. A slower lithiation can be expected to form a relatively more even strain–stress distribution and a more homogeneous charge-transfer active area, leading to lower R_{ch-tr} values for the prelithiated cells.^[11,33] As displayed in Figure 3e, the differences in terms of $R_{SEI/CEI}$, R_{ic} , and R_{ch-tr} are quite remarkable for both type of cells during the first ten cycles, showing a clear advantage for the cell prelithiated using PLMP.^[43]

The averages of the three selected measurements, along with their corresponding standard deviations, are reported in Table S1,

Supporting Information. Furthermore, distribution of relaxation times (DRT) data supporting the fitting results are provided in Figure S1, Supporting Information, where the SEI-related resistance and the CEI-related resistance can be more clearly distinguished (τ : 10^{-6} – 10^{-2} s).

2.2. Postmortem Analyses

2.2.1. Morphology Analyses by FE-SEM

As previously discussed, in regular LIB cells, the SEI and CEI form by gradual reduction/oxidation of the electrolyte components during the initial cycles whereas the sudden decrease in potential of the prelithiated SiGr electrode causes simultaneous reduction of all electrolyte components. To observe how this difference affects the surface morphologies, SiGr and NMC-811 electrodes were

investigated by scanning electron microscopy (SEM) (Figure 4) after long-term cycling (300 cycles). Closeup images of the same materials can be found in our previous publication.^[23] Figure 4a shows the pristine SiGr electrode composed of smaller SiGr composite particles among the larger Gr particles that have flake-like shapes and sharp edges (Figure S2, Supporting Information). As can be seen from Figure 4b,c, Gr particles at the surface are less visible and the surfaces are rougher after 300 cycles for both non-prelithiated and prelithiated SiGr electrodes as electrode surface is covered with a whiteish layer which was not attributed to salt remains as all electrodes were washed with DMC prior to analyses. Moreover, a visible increase in particle size can be observed for both SiGr electrodes. Despite being smoother and having a more similar appearance to the pristine electrode, lower interstitial porosity between the particles demonstrates a thicker SEI layer at the surface of the prelithiated SiGr electrode (Figure 4b). Although a too thick SEI layer is not desirable on electrodes as it may increase the cell impedance, Si-containing electrodes require a mechanically stable interphase layer. Thus, having a thicker SEI on the prelithiated SiGr electrodes is not necessarily a disadvantage as it can endure the volume changes and limit the irreversible active material loss during cycling.

Even though only the negative electrode was lithiated in the prelithiated cell prior to cycling, its effect on long-term cycling affected the CEI formation on the NMC-811 electrode. Figure 4d shows the surface of a pristine NMC-811 electrode where the secondary NMC-811 particles and the interstices between the particles are visible (Figure S3, Supporting Information). When Figure 4e,f is compared, the CEI layer appears

to be much thicker for the nonprelithiated cell after 300 cycles covering most of the electrode surface whereas particle boundaries are much more visible for the NMC-811 electrode cycled against the prelithiated SiGr electrode. NMC-811 electrodes cycled in the prelithiated and nonprelithiated cells reached a similar end of charge (EoC) potential after 300 cycles (Figure S4 and S5, Supporting Information), thus similar oxidation components are expected to form on both electrodes. However, the minimum and maximum electrode potentials attained by the NMC-811 electrode are much higher in the nonprelithiated cell compared to the prelithiated one. Higher average electrode potentials result in oxidation of more electrolyte components on the electrode surface, forming a thicker and more resistive CEI layer throughout cycling.

The impedance measurements show that prelithiation using PLMP is beneficial for the formation of superior, in terms of resistivity, interphase layers on SiGr electrodes as well as on the CEI formation on NMC-811 since it strongly affects the potential ranges of the two electrodes throughout cycling. To shed light on how cycling performance can be improved by prelithiation, its effect on the formation of the interphase films is further analyzed via XPS analysis.

2.2.2. Interphase Composition Analyses by XPS

Effects of prelithiation on the interphases on SiGr and NMC-811 electrodes are evaluated by XPS analyses, and the corresponding organic and inorganic components in the interphases are shown in Table 1.

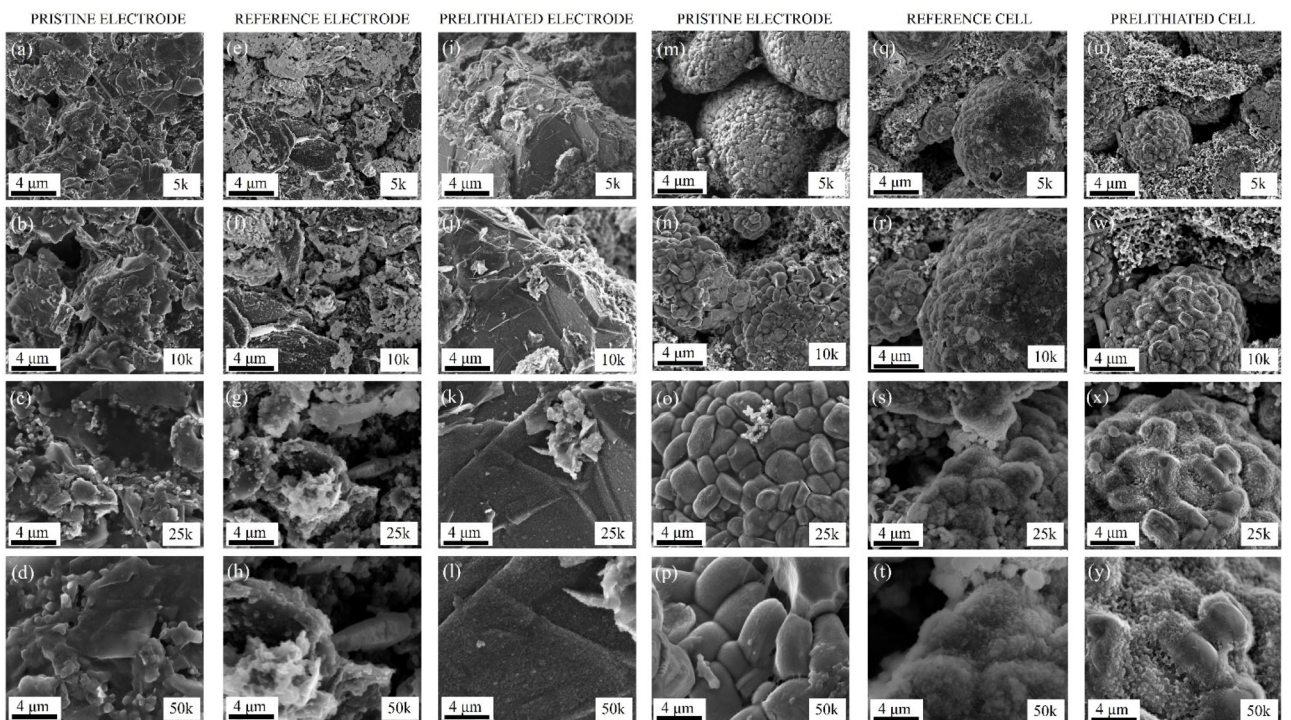


Figure 4. SEM images of a–d) pristine SiGr electrode, e–h) cycled SiGr electrode, i–l) cycled prelithiated SiGr electrode, m–p) pristine NMC-811 electrode, q–t) NMC-811_n electrode, and u–y) NMC-811_p electrode (cycle number: 300 following formation, 1C/1D Signal A: InLens, EHT: 3 kV, magnification: 5–50 kx).

Table 1. Binding energy XPS signals of assigned inorganic and organic components of the interphase films on SiGr and NMC-811 electrodes after cycling.				
F_{1s}	F1 LiF (685–686 eV) ^[49,51]	F2 PVdF (687.6 eV) ^[49] /Fluorine-carbon (\approx 687 eV) ^[63] Li _x PO _y F _z (\approx 687.2 eV) ^[44] Li _x PF _y O _z + Li _x PF _y (\approx 688.3 eV) ^[51]	F3 C _x F _n (688–689 eV) ^[64]	
Li_{1s}	Li1 LiOH (\approx 54.9 eV) ^[65] Li ₃ PO ₄ (\approx 55.5 eV) ^[66] Li ₂ CO ₃ , EtOCO ₂ Li (\approx 55.4 eV) ^[66,67] Li ₂ O (55.6 eV) ^[65]		Li2 LiF (55.9–56.2 eV) ^[65,67]	
P_{2p}	P1 Li ₃ PO ₄ (133.6 eV) ^[68,69] Poly-phosphate P–O–P (\approx 134 eV) ^[44,45]		P2 Li _x PF _y O _z (135.2–136 eV) ^[49,51] Li _x PF _y /PF _y (137–138 eV) ^[49,64]	
O_{1s}	O1 Li ₂ O (<530 eV) ^[44,70] M–O species in pristine NMC (529.3 eV) ^[49]	O2 Poly-ether (\approx 531.3 eV) ^[66] Li ₃ PO ₄ (532.0 eV) ^[69] Lithium alkyl carbonate (531.8 and 533.3 eV) ^[67] Li ₂ CO ₃ (531.5 eV/532.4 eV) ^{[70]/[49]} Oxidized conductive C (531.5 eV) ^[49] C=O (531.5–532 eV) ^[64]	O3 Graphite (532.7 eV) ^[71] Oxyfluorinated carbon (\approx 533.0 eV) ^[63] C–O species (532.5–533.5 eV) ^[44,64] Hydroxyl groups (\approx 533.2 eV) ^[72]	O4 RCO ₃ (534.1 eV) ^[49] Epoxides (\approx 534.4 eV) ^[72] R–CF ₂ –O–CF ₂ –R (535.7 eV) ^[73]
C_{1s}	C1–C6 Graphite/hydrocarbon C–C and conductive C (284.1–284.8 eV) ^[49,50] (C1), C–H (284.8–285.2 eV) ^[64] (C1), poly-ether carbon C–O and CH ₂ (286.0*–286.9 eV) ^[50,64] (C2), RCO ₃ (287.3 eV) ^[49] C–O–C ethers (C3), C=O (287.6–289.0 eV) ^[64] (C4), O–C=O such as in Li ₂ CO ₃ (289 eV) ^[66] (C5), semi-carbonates (R–CH ₂ OCO ₂ Li from LiPF ₆ , 289.4 eV) ^[50] (C5), π – π^* satellite peak from aromatic carbons (291 eV) ^[74] (C6), CH ₂ (286 eV) (C2) and CF ₂ (291 eV) (C6) in the PVdF binder. ^[46] (CF ₂ –CH ₂ (286.9 eV), C–F (290.6 eV)			

The elemental composition (C, O, Li, F, P, N, and S) of the interphases is shown after the formation cycles (Figure 5a,c and 6a,c) and after long-term cycling (300 cycles at 1C/1D, Figure 5b,d and 6b,d) for the outermost layers and for various sputtering depths (0–96 nm) which, from here on, will be denoted as surface (5–10 nm) and SEI/CEI interlayers (10–96 nm), respectively. Additionally, analyses of the high-resolution core level spectra of each element (Figure S6–S13, Supporting Information) were carried out for the electrode surfaces (5–10 nm) for a more elaborate understanding of each SEI and CEI components.

2.2.2.1. Interphase Composition after Formation Cycles

Postformation SEI on SiGr Electrodes [S_{1s} & P_{2p}] Sulfur was detected only at the surface (<0.4%_{at.}) for both nonprelithiated and prelithiated SiGr electrodes, regardless of cycling time (post-formation or after 300 cycles). This indicates that reduction products of LiTFSI, as Li₂S or Li₂SO₄, contribute negligibly to the SEI. Despite the high LiPF₆ concentration (1 M) in the electrolyte, phosphorus was among the least abundant elements, with \approx 2%_{at.} at the surface and 1–1.5%_{at.} in the SEI interlayers. Li₃PO₄ and polyphosphates (P1) were more prominent than Li_xPF_yO_z, LiPF_y, or PF_y (P2).^[44,45] Since electrolyte components reduce simultaneously on prelithiated electrodes, LiPF₆ reduction products in the SEI are expected to be dominated by LiF. A detailed discussion of this mechanism is provided in our earlier work (Figure 4b in).^[23]

[O_{1s}] O_{1s} signals arise from both inorganic (e.g., Li₂O, Li₂CO₃) and organic SEI species, complicating assignments. Prior studies show that outer SEI layers are mainly organic.^[46] Consistently, the nonprelithiated electrode showed higher O_{1s} (21.6%_{at.}) and C_{1s}%_{at.} at the surface compared to the prelithiated electrode (O_{1s}: 12.8%_{at.},

suggesting a more organic-rich surface. The dominant O2 contribution indicates polyethers, lithium alkyl carbonates, and possibly Li₂CO₃. Additives such as FEC and VC generate polyethers (e.g., cross-linked polyethylene oxide) that improve SEI stability on Si-based anodes,^[47] though at the expense of ICE due to higher Li consumption. The O3 contribution (fluorinated C, CO, carbonyl groups) was the second most significant, while O4 (epoxides, fluorinated ethers) was minor. With sputtering to 32 nm, O_{1s}%_{at.} decreased and stabilized, consistent with fewer organic species near the electrode surface.^[48]

[C_{1s}] The pristine SiGr electrode showed 85.2%_{at.} C_{1s} at the surface (Figure S2, Supporting Information), which decreased to 33%_{at.} (nonprelithiated) and 29%_{at.} (prelithiated) after formation. Graphitic carbon and electrolyte components contribute C_{1s} signals between 284 and 291 eV (Table 1). The C1 peak (graphite, C–C, conductive C, 284.1–284.8 eV)^[49,50] dominated, accounting for \approx 83% of all C species. C2 and C3 peaks (ethers, alkyl carbonates, and small amounts of R–CH₂OCO₂Li)^[50] were also present, consistent with electrolyte reduction products (LiPF₆, DMC, DEC, EC).^[47,51,52] Fluorinated carbons (e.g., CF₂, \approx 291 eV, C6)^[44] were not observed at either overlayer. At all depths, the prelithiated SiGr electrode exhibited lower C_{1s}%_{at.} (Figure 5a,b), indicating less carbonaceous SEI formation at lower electrode potentials. This agrees with EIS results, where inorganic SEI species formed at low potentials are reported to be more conductive and mechanically robust.^[36]

[Li_{1s}] After formation, Li_{1s}%_{at.} was higher for the prelithiated electrode (34.9%_{at.}) than for the nonprelithiated one (25%_{at.}). At the surface, LiF (Li2) accounted for 25%_{at.} (nonprelithiated) and 31%_{at.} (prelithiated), with an additional \approx 4%_{at.} from Li₃PO₄ and Li₂CO₃ (Li1). In the SEI interlayers, the prelithiated electrode consistently showed 5–10%_{at.} higher Li_{1s}%_{at.}, confirming an SEI richer in inorganic species. This agrees with reports that LiF forms

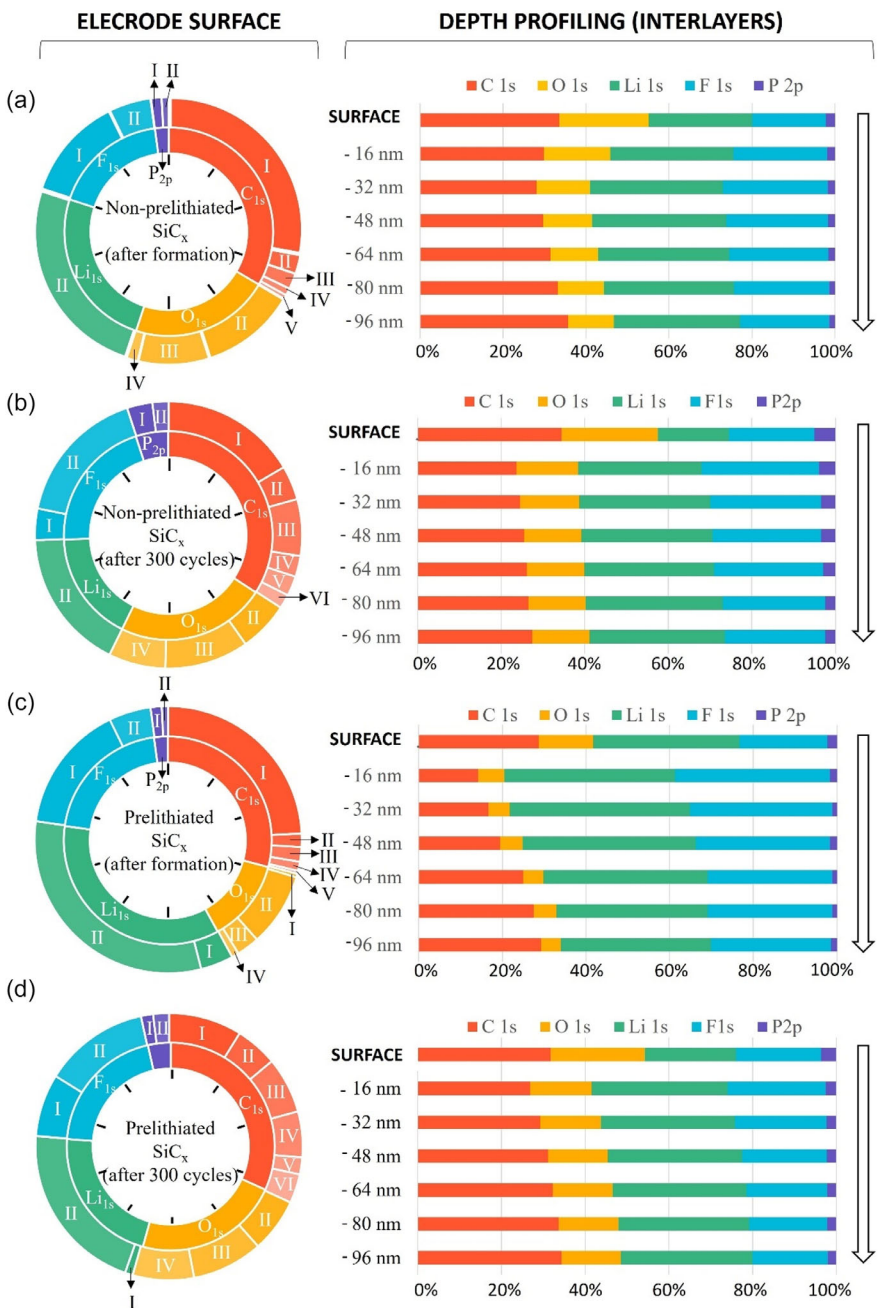


Figure 5. Elemental composition (%_{at}) of the overlayer and interlayers in SiGr: a) Nonprelithiated and c) Prelithiated electrodes after formation cycles (1x C/10, 3x C/3). b) Nonprelithiated and d) Prelithiated electrodes after 300 cycles (1C rate, following formation). All cells were stored at 40 °C for 7 days prior to cycling. (T_{cycling}: 20 °C). The “Surface” corresponds to ≈5 nm, and the SEI interlayers correspond to 16–96 nm. Elemental concentrations are normalized to 100 atomic%. Each section on the pie charts represent 10% of elemental composition.

readily on lithiated Si in the presence of FEC, improving adhesion between Li_xSi and LiF.^[16,53,54]

[F_{1s}] At the surface, F_{1s} was 17.8%_{at} (nonprelithiated) and 20.5%_{at} (prelithiated) after formation. Li_xPF_yO_z and Li_xPF_y (F2) accounted for ≈5%_{at} of all F species on both electrodes. A higher F1 contribution was consistent with Li_{1s} data, indicating a LiF-rich SEI in the prelithiated electrode (15.4%_{at}) compared to the nonprelithiated one (12.7%_{at}). At the SEI interlayers, F_{1s}%_{at} was higher than at the surface, especially for the prelithiated electrode, reflecting greater inorganic enrichment near the electrode.

Postformation CEI on NMC-811 Electrodes XPS analyses were performed to characterize CEI formation on NMC-811 electrodes after formation cycles. Elemental distributions at the surfaces and interlayers are shown in Figure 6a,c, with high-resolution spectra in Figure S6–S12, Supporting Information. We remind the readers that, for clarity, NMC-811 cycled against nonprelithiated SiGr is denoted as NMC-811_n and against prelithiated SiGr as NMC-811_p. The pristine electrode surface contained C (49%_{at}), F (31.6%_{at}), O (11.9%_{at}), and Li (6.6%_{at}), along with Mn, Co, and Ni (Figure S3, Supporting Information).

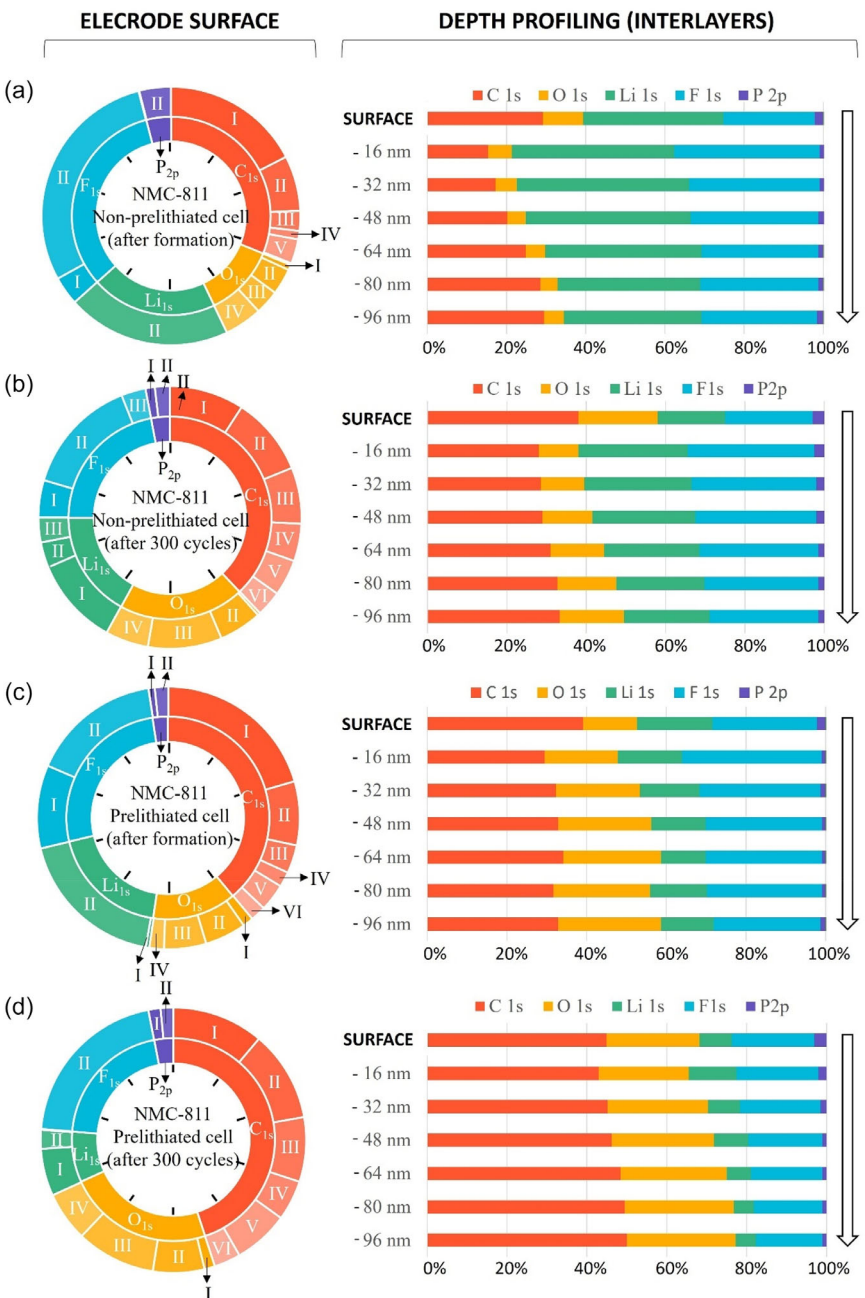


Figure 6. Elemental composition (%_{at}) of the overlayer and interlayers in NMC-811: a) NMC-811_n and c) NMC-811_p after formation cycles (1x C/10, 3x C/3). b) NMC-811_n and d) NMC-811_p after 300 cycles (1C rate, following formation). All cells were stored at 40 °C for 7 days prior to cycling. ($T_{cycling}$: 20 °C). The "Surface" corresponds to \approx 5 nm, and the SEI interlayers correspond to 16–96 nm. Elemental concentrations are normalized to 100 atomic%. Each section on the pie charts represents 10% of elemental composition.

[P_{2p}] Sulfur appeared only after formation, at 0.4%_{at} for NMC-811_n and 0.2%_{at} for NMC-811_p. Phosphorus was 2.4%_{at} on NMC-811_p, mainly as Li_xP_yO_z, LiPF_y, and PF_y (P2), with minor Li₃PO₄ and polyphosphates (P1). On NMC-811_n, P was higher (4%_{at}) but lacked P1 contributions. In both electrodes, P_{2p} content dropped to 0.5%_{at} after the first ablation (16 nm) and remained constant with further sputtering to 96 nm.

[C_{1s}] After CEI formation, surface C_{1s} decreased to 30.9%_{at} (NMC-811_n) and 38.5%_{at} (NMC-811_p). Interpretation is complicated by overlapping of PVDF with polyethers and aromatic

carbons.^[46] On pristine electrodes, PVDF contributed strongly (C2: 18.2%_{at}, C6: 12.3%_{at}). After formation, C2 decreased to 6.9%_{at} (NMC-811_n) and 7.8%_{at} (NMC-811_p), while C6 decreased to 0.2 and 1.9%_{at}, respectively. This suggests a thicker CEI on NMC-811_n. New C3 and C5 signals (ethers, alkyl carbonates, semi-carbonates) appeared on both electrodes after formation. At the interlayers, C_{1s} stabilized at 30–35%_{at} for both cathodes.

[O_{1s}] Surface O_{1s} levels were comparable to the pristine electrode. However, O2 contributions decreased, while –OH, –CO, and oxyfluorinated carbons (O3) increased. Alkyl carbonates,

epoxides, and fluorinated ethers (**O4**) were also detected, contributing 1.8%_{at.} on NMC-811_n and 4.7%_{at.} on NMC-811_p. Despite this difference, O_{1s} composition in the interlayers was similar for both electrodes, increasing slightly after initial sputtering (0–64 nm) and then remaining constant.

[Li_{1s}] Surface Li_{1s} nearly tripled compared to the pristine electrode (6.6%_{at.}). LiF (**L1**) was the dominant Li species on both electrodes, with an additional 0.4%_{at.} Li1 detected on NMC-811_p. In the interlayers, Li_{1s} remained ≈20%_{at.} for NMC-811_n but decreased gradually to 12–15%_{at.} for NMC-811_p.

[F_{1s}] Surface F_{1s} was 32.3%_{at.} on NMC-811_n and 26.0%_{at.} on NMC-811_p. Both electrodes were dominated by Li_xPF_yO_z and Li_xPF_y, but NMC-811_p showed ≈3× higher relative LiF contribution. Higher LiF content is considered beneficial, as it suppresses side reactions between ethers and the cathode surface.^[1] Binder interference complicates interlayer analysis, as PVdF signals overlap with LiPF₆ reduction products.^[49] Nonetheless, interlayers of NMC-811_p contained ≈5%_{at.} more F compared to NMC-811_n.

Summary for Postformation SEI and CEI The SEI on SiGr and the CEI on NMC-811 electrodes showed complementary trends influenced by prelithiation. On the anode side, prelithiation promoted the formation of inorganic-rich SEI layers, particularly LiF, while reducing the contribution of carbonaceous species. On the cathode side, electrodes paired with prelithiated SiGr (NMC-811_p) also exhibited LiF-enriched CEI with thinner interphases, compared to the thicker, more organic-rich CEI observed for NMC-811_n. These results indicate that prelithiation not only stabilizes the anode SEI but also indirectly influences CEI composition, leading to interfaces richer in inorganic species that are generally more robust and less resistive. Together, these findings highlight the coupled evolution of SEI and CEI chemistries and their collective impact on full-cell stability.

2.2.2.2. Interphase Composition after 300 Cycles

Aged SEI on SiGr Electrodes [P_{1s}] After 300 cycles, nonprelithiated electrodes showed a higher contribution from Li₃PO₄ and polyphosphates (**P1**) compared to Li_xPF_yO_z, LiPF_y, and PF_y (**P2**). Relative phosphorus content nearly doubled in prelithiated electrodes and almost tripled in nonprelithiated electrodes compared to postformation, indicating ongoing electrolyte consumption for SEI repair, which was more severe without prelithiation.

[O_{1s}] Both electrode types showed increased O_{1s} content and greater **O4** contributions, consistent with the accumulation of more stable epoxides and fluorinated ethers during extended cycling.

[C_{1s}] In the SEI interlayers of prelithiated electrodes, relative C_{1s} content was larger compared to postformation. Okuno et al. reported that LiF can act as a ‘glue’ between lithiated Si and organic SEI species, as Li in Li_xSi bonds with F in LiF aggregates.^[53] Thus, higher LiF formation during prelithiation likely enhanced the incorporation of carbonaceous species into the SEI after long-term cycling, suggesting improved mechanical stability.

[F_{1s}] A key difference after 300 cycles was the higher contribution of **F2** relative to **F1** at the electrode surfaces, reflecting

accumulation of Li_xPF_yO_z and Li_xPF_y species. **F2** accounted for 17.8%_{at.} of all surface components in nonprelithiated electrodes and 9.1%_{at.} in prelithiated electrodes.

Summary for Postformation and Aged SEI Comparison of postformation and aged SEI reveals a clear evolution in interphase chemistry. While prelithiation initially promoted the formation of inorganic-rich, LiF-dominated SEI with fewer carbonaceous components, long-term cycling led to increased contributions from phosphates, epoxides, fluorinated ethers, and carbon-containing species. These trends suggest that continued electrolyte decomposition sustains SEI repair, more prominently in nonprelithiated electrodes, whereas prelithiated electrodes maintain a more stable balance between inorganic and organic components. Together, the results highlight how prelithiation not only shapes the initial SEI but also governs its long-term chemical and mechanical stability.

Aged CEI on NMC-811 Electrodes Elemental compositions of the surfaces and CEI interlayers after 300 cycles at 1C/1D are shown in Figure 6c–d.

[P_{2p}] Both **P1** and **P2** species were detected at the surfaces after long-term cycling, with a slight (≈1%_{at.}) increase in P_{2p} content at the interlayers.

[C_{1s}] Surface C_{1s} increased by ≈7%_{at.} compared to postformation, indicating accumulation of C-containing species. After 300 cycles, **C4** and **C6** contributions were comparable, while **C1**, **C2**, **C3**, and **C5** were slightly higher for NMC-811_p than NMC-811_n. Combined with SEM results (Figure 4) and relative O_{1s}, Li_{1s}, and F_{1s} levels, this suggests a thinner interphase on NMC-811_p.

[O_{1s}] Surface O_{1s} increased by ≈10%_{at.} for both electrodes. Carbonates (**O2**) were dominant, along with oxyfluorinated carbon and hydroxyl species. Epoxides and fluorinated ethers contributed ≈5.4%_{at.} at the surface. At each interlayer, O_{1s} content was 10–15%_{at.} higher for NMC-811_p compared to NMC-811_n.

[Li_{1s}] After 300 cycles, surface Li_{1s} decreased to 17%_{at.} (NMC-811_n) and 8%_{at.} (NMC-811_p). Li1 species (Li₂CO₃, Li₃PO₄, Li₂O) contributed ≈3%_{at.} at the surface, while LiF remained the dominant Li-containing species. Across the interlayers, Li_{1s} content was 15–19%_{at.} for both electrodes, indicating a relatively Li-rich inorganic CEI on NMC-811_n.

[F_{1s}] The surface of NMC-811_n contained LiF (**F1**), Li_xPF_yO_z (**F2**), and fluorinated carbon (**F3**), whereas NMC-811_p showed only **F2** species. Surface F content was ≈10%_{at.} lower for NMC-811_p, consistent with a thinner interphase compared to NMC-811_n.

Comparison of postformation and aged CEI highlights significant interphase evolution during long-term cycling. While both electrodes initially formed LiF-containing CEI, extended cycling led to higher accumulation of carbonates, fluorinated ethers, and phosphate species. The NMC-811_n electrode developed a thicker, more inorganic- and F-rich interphase, whereas NMC-811_p maintained a thinner CEI with relatively lower Li and F contributions. These results suggest that pairing with a prelithiated anode not only influences initial CEI composition but also suppresses excessive CEI growth during extended operation, contributing to improved cathode stability.

2.2.2.3. Conclusions of Interphase Characteristics

[SEI] LiF within the SEI of Si-containing electrodes improves ductility by forming stable delocalized void structures^[53] while suppressing parasitic reactions.^[55] Thus, a LiF-rich SEI is highly beneficial for SiGr electrodes. The results demonstrate that LiF-rich interphases can be achieved without using salts with strong Li⁺ coordination (e.g., LiClO₄, LiBF₄), which are known to impair coulombic efficiency^[56] and increase impedance. Instead, weakly coordinating salts (e.g., LiPF₆, LiTFSI) combined with prelithiation via PLMP yield a similarly LiF-rich SEI, benefiting both CE and capacity retention.^[57]

Additionally, Li₂CO₃, being more insulating than LiF, reacts with Li to form Li₂O at the innermost SEI layer.^[58–60] The resulting Li₂O, a wide bandgap insulator, helps limit SEI thickening and impedance rise over long-term cycling. Prelithiation also promoted Li₃PO₄ formation, which improves rate capability due to its high ionic conductivity and chemical inertness across wide potential and temperature ranges.^[60] Continuous electrolyte reduction (mainly LiPF₆) persisted during cycling, with more severe repair demands on nonprelithiated electrodes. Literature reports confirm that decomposition of LiPF₆ generates acidic species (e.g., F₂PO₂H) that damage the organic SEI (e.g., LEDC), accelerating capacity decay.^[61,62] The reduced accumulation of such species (F2) in prelithiated electrodes indicates formation of a superior, more diverse SEI that better supports long-term stability.

[CEI] Changes in surface C_{1s} and O_{1s} content after 300 cycles indicate a thinner CEI on NMC-811_p than on NMC-811_n, consistent with SEM observations. This effect is attributed to the lower average electrode potential reached by NMC-811 when cycled against a prelithiated anode. Li_{1s} analysis further confirmed reduced LiF and thinner CEI formation on NMC-811_p compared to NMC-811_n. Specifically, LiF contributions differed significantly (13.9% for NMC-811_n vs 5.7% for NMC-811_p).

Cycle-life data further support this interpretation as the prelithiated full-cell completed 300 cycles (1C/1D rate) in ≈950 h, whereas the nonprelithiated cell failed after ≈600 h.^[23] EoC potentials were similar (4.24 V for NMC-811_n, 4.2–4.30 V for NMC-811_p), suggesting broadly comparable CEI chemistry dominated by electrolyte oxidation. However, the consistently higher average potentials attained by NMC-811_n caused more extensive electrolyte oxidation and thicker CEI buildup compared to NMC-811_p (Figure S4 and S5, Supporting Information).

3. Conclusion

Within this work, effects of prelithiation (of the negative electrode) using PLMP on cell impedance and interphase films on SiGr and NMC-811 electrodes are investigated. In summary, PLMP method improves the total cell impedance in NMC-811 || SiGr cells as it decreases the impedance related to interphase films by promoting a more diverse SEI layer consisting of beneficial components such as LiF and Li₃PO₄. Additionally, charge transfer and contact resistance are decreased as a result of the formation of a more homogeneous SEI with a more even

strain–stress distribution. Moreover, PLMP helps removing the trace amount of H₂O in the cells, further benefitting the cells in terms of contact resistance. SEM images show a thicker interphase layer with less interstitial porosity forms on the prelithiated SiGr electrode. Moreover, a thinner CEI forms on the NMC-811 electrodes due to lower average potentials attained by the positive electrode throughout long-term cycling, which is also supported by the relative O_{1s}, Li_{1s}, and F_{1s}%_{at.} measured by the XPS analyses. Furthermore, it is shown by the XPS analyses that LiPF₆ mainly contributes to the SEI as LiF and P-free organic components are only a small percentage of phosphorus-containing products present at the surfaces and SEI interlayers of the SiGr electrodes after the formation cycles. However, while being less severe for the prelithiated cell, Li_xP_yO_z, LiP_yF_z, and PF_y components at the surface increase over long-term cycling due to SEI reparation, showing continuous electrolyte reduction on the negative electrodes in both cells. Furthermore, it is shown that the SEI layer forming at lower potentials (as on prelithiated SiGr electrode) contains less C-containing components and is relatively richer in inorganic components (i.e., LiF) at the surface as well as the SEI interlayers. It is evident that prelithiation using PLMP does not only improve the cycling performance by providing a lithium reservoir, but it also manipulates the interphases on the SiGr, and positive electrodes cycled against them. Thus, it is an auspicious method to improve electrochemical performance of Li-ion batteries via engineering of the interphase films.

4. Experimental Section

Material Preparation: Electrodes

The positive electrodes were prepared using NMC-811 (95%, T81R, Targray) as active material, carbon black (2%, C-NERGY Super C-65, IMERYS) as the conductive additive, and polyvinylidene difluoride (3%, PVDF Solef 5130, Solvay) as the binder. N-methyl pyrrolidone was used as the solvent for slurry preparation to which first PVDF, then Super C65, and finally NMC-811 powder was added under continuous stirring. When homogeneous distribution was ensured, the slurry was cast on an aluminum foil (Hydro, 20 µm) and calendared to 3.2 g cm⁻³ (thickness: 85 ± 2 µm). Mass loading of the prepared NMC-811 electrodes was 21.0 ± 0.3 mg cm⁻² (4.0 mAh cm⁻²) and had a specific capacity of 200 mAh g⁻¹_{NMC-811}. Finally, electrodes were dried under vacuum for 16 h at 120 °C prior to cell assembly.

The negative electrodes were prepared using a SiGr composite (94%) as the active material and C-65 (1%) as the conductive additive along with a binder mixture composed of styrene-butadiene rubber (SBR, 3%) and carboxymethyl cellulose (CMC, 2%). The slurry was cast on a copper foil (thickness: 10 µm) and calendared to 1.4 g cm⁻³ (thickness: 48 ± 1 µm). The mass loading of the prepared SiGr electrodes was 6.6 mg cm⁻² (4.2 mAh cm⁻²) and they had a specific capacity of 636 mAh g⁻¹. Finally, the prepared electrodes were dried under vacuum for 24 h at 80 °C prior to cell assembly.

Electrolyte Preparation

The main conductive salt in the electrolyte was 1 M lithium hexafluorophosphate (LiPF₆, ENCHEM, purity: 99.8%). It was dissolved in a

mixture of diethyl carbonate (DEC, Soulbrain, purity: 99.98%), dimethyl carbonate (DMC, BASF, purity: 99%), ethylene carbonate (EC, Merck, battery grade), and fluoroethylene carbonate (FEC, Solvay, purity: 99.9%) (wt 3:3:3:1). The electrolyte additionally contained 0.5 wt% lithium bis(trifluoromethanesulfonyl)imide (LiTFSI, 3 M, battery grade), and 2 wt% vinylene carbonate (VC, BASF, battery grade), and 1 wt% trifluoroethylacetate (Solvay, battery grade) as additives.

Prelithiation of SiGr Electrodes

Prelithiation was done using PLMP (China Energy Lithium) at 2.5 wt% with respect to the weight of NMC-811, which corresponds to 48.2% of the capacity of the NMC-811 cathode. The diameter of the PLMP particles varied between 20 and 50 μm and each particle had a $\approx 1 \mu\text{m}$ thick Li_2CO_3 interphase layer which was disregarded for the capacity calculation. The PLMP was dispersed on the electrode surface using a spatula. The covered electrodes were then hand pressed under a mylar foil to break the Li_2CO_3 interphase layer. The whole process was completed in an argon-filled glove box ($\text{O}_2 < 0.5 \text{ ppm}$, $\text{H}_2\text{O} < 0.5 \text{ ppm}$).

For clarity, NMC-811_n refers to NMC-811 cycled against nonprelithiated SiGr, and NMC-811_p to NMC-811 cycled against prelithiated SiGr.

Electrochemical Investigations

EIS measurements were performed using a Bio-logic VMP III potentiostat/frequency response analyzer in a frequency range of 1 MHz–0.1 Hz (amplitude: 10 mV) for prelithiated and nonprelithiated NMC-811||SiGr cells after each charge and discharge steps for ten cycles. 2032-type coin cells were prepared in an argon-filled glove box ($\text{O}_2 < 0.5 \text{ ppm}$, $\text{H}_2\text{O} < 0.5 \text{ ppm}$) using the aforementioned NMC-811 positive electrodes ($\phi: 12 \text{ mm}$) coupled with prelithiated or nonprelithiated SiGr anodes ($\phi: 13 \text{ mm}$). Microporous Celgard 2500 separators (dried at 60 °C under vacuum for 24 h) wetted with electrolyte (100 μL) were used for all measurements and all cells were stored at 40 °C for 7 days in a climatic chamber (KB400, BINDER GmbH) prior to measurements. Galvanostatic charge and discharge steps (4.2–2.8 V) between the EIS measurements were carried out with the same Bio-logic VMP III to enable continuous measurements for ten cycles. The current rate (C-rate) was set as C/10 for the initial charge and discharge steps, and it was increased to C/3 for the subsequent nine cycles. DRT analysis (regularization parameter $\lambda: 10^{-5}$) was performed using the RelaxIS software to determine the number of resistance (R) and constant phase elements (CPE). The investigated system was then represented by an equivalent circuit consisting of a bulk resistance element (R_b); connected in series with three Randles cells made of CPE and resistors (R) in parallel, corresponding to interphase resistance ($R_{\text{SEI/CEI}}$), electronic contact resistance (R_{ic}), and charge transfer resistance ($R_{\text{ch-tr}}$). Furthermore, a Warburg element (W) was included to account for the impedance caused by Li diffusion in the bulk of the electrodes. Consequently, the equivalent circuit impedance used to describe the assembled cells and fit the EIS spectra was $Z = R_b + R_{\text{SEI/CEI}}\text{-CPE}_{\text{SEI/CEI}} + R_{\text{ic}}\text{-CPE}_{\text{ic}} + R_{\text{ch-tr}}\text{-CPE}_{\text{ch-tr}} + W$. Area normalization is done by considering only the working electrode ($\phi: 12 \text{ mm}$).

The long-term galvanostatic charge/discharge measurements were performed using a MACCOR series 4000 battery cycler. 2032-type coin cells (minimum 3 cells per condition) identical to the ones used for EIS measurements were assembled in an argon-filled glove box ($\text{O}_2 < 0.5 \text{ ppm}$, $\text{H}_2\text{O} < 0.5 \text{ ppm}$) and stored at 40 °C for 7 days in a climatic chamber (KB400, BINDER GmbH) prior to the measurements. After this storage period, all cells were placed in another climatic

chamber at 20 °C and cycled 300 times between the cutoff voltages of 4.2 and 2.8 V using constant current/constant voltage charging steps (CCCV) and constant current discharging (CC) steps. The formation step consisted of one cycle at (C/10; 0.05C) and three subsequent cycles at C/3. After the formation cycles, the current rate was increased to 1C (CCCV, 1C, $I < 0.05\text{C}$) for the rest of the cycling.

Morphology Analyses

The morphology of the prelithiated and nonprelithiated SiGr electrodes was investigated using an Auriga FE-SEM with a Schottky field emission gun (Carl Zeiss) as the electron source. The accelerating voltage for the in-lens secondary electron detector was 3 kV with a working distance of 3 mm. Cells were disassembled after 300 cycles in an argon-filled glove box ($\text{O}_2 < 0.5 \text{ ppm}$, $\text{H}_2\text{O} < 0.5 \text{ ppm}$) and each electrode was washed with 300 μL DMC to remove the salt residues. Finally, dried electrodes were placed in an air-tight (vacuum-sealed) sample holder to avoid contact with air and moisture during their transfer to the device.

Interphase Composition Investigations

The impact of prelithiation on interphase films (SEI and CEI) were investigated by XPS measurements performed after the formation cycles and after 300 cycles. A Thermo Fisher VG Scientific type K-Alpha XPS device calibrated on gold, silver, and copper references was used for the measurements. A monochromatic Al Ka source was used for the measurements and the pass energy of high-resolution core spectra and survey spectra was 30 and 200 eV, respectively. A charge neutralizer was used to compensate for the sample charging. The disassembly of all cells was done in an argon-filled glove box ($\text{O}_2 < 0.5 \text{ ppm}$, $\text{H}_2\text{O} < 0.5 \text{ ppm}$) and all electrodes were rinsed with 300 μL DMC. Dried samples were attached to an air-tight sample holder using a two-sided carbon tape for their transfer to the device. Data fitting was performed via the CasaXPS software with an internal reference (F_{1s} peak at 685.0 eV). Sputter depth profiling was done with monoatomic argon ions for precise determination of the sputtering depth. The modified Scofield sensitivity factors used to calculate atomic concentration percentages (%_{at}) were 4.117647, 2.880686, 1.0, 1.294118, 1.352941, 0.06098681, and 1.676146 for F_{1s} , O_{1s} , C_{1s} , S_{2s} , P_{2p} , Li_{1s} and N_{1s} peaks, respectively. Although the estimation of the sputter depth was possible, since monoatomic argon ions might change the oxidation state of the elements, only the total %_{at} of each element was measured and the individual contributions (i.e., C1, C2, C3, etc.) were not investigated.

Acknowledgements

The research reported is part of the "SPIDER" project funded by the European Union's Horizon 2020 research and innovation program under grant agreement no. 814389. Financial support from the German Federal Ministry of Education and Research for Dr. Masoud Baghernejad within the project "EFoBatt" (grant no. 13XP5129) is gratefully acknowledged.

Open Access funding enabled and organized by Projekt DEAL.

Conflict of Interest

The authors declare no conflict of interest.

Author Contributions

Masoud Baghernejad: formal analysis (supporting); methodology (supporting); supervision (lead); writing—review and editing (supporting). **Ekin Esen:** conceptualization (lead); data curation (lead); formal analysis (lead); funding acquisition (lead); investigation (lead); methodology (lead); software: (lead); validation (lead); visualization (lead); writing—original draft (lead). **Iratxe de Meatza:** data curation (supporting); formal analysis (supporting); validation (supporting); writing—review and editing (supporting). **Martin Schmuck:** formal analysis (supporting); investigation (supporting); writing—review and editing (supporting). **Mohsen Padervand:** validation (supporting); writing—review and editing (supporting). **Martin Winter:** project administration (supporting); supervision (supporting); visualization (supporting); writing—review and editing (supporting). **Elie Paillard:** conceptualization (supporting); project administration (lead); supervision (supporting); visualization (supporting).

Data Availability Statement

The data that support the findings of this study are available from the corresponding author upon reasonable request.

Keywords: cathode electrolyte interphase • passivated lithium metal powder • prelithiation • silicon carbon composite electrodes • solid electrolyte interphase

- [1] A. J. B. Goodenough, A. Manthiram, *MRS Commun.* **2014**, *4*, 135.
- [2] R. Schmuck, R. Wagner, G. Höppl, T. Placke, M. Winter, *Nat. Energy* **2018**, *3*, 267.
- [3] S. Goutam, N. Omar, P. Van Den Bossche, J. Van Mierlo, *Emerging Nanotechnol. Rechargeable Energy Storage Syst.* **2017**, *45*.
- [4] K. Marker, P. J. Reeves, C. Xu, K. J. Griffith, C. P. Grey, *Chem. Mater.* **2019**, *31*, 2545.
- [5] L. Y. Beaulieu, T. D. Hatchard, A. Bonakdarpour, M. D. Fleischauer, J. R. Dahn, *J. Electrochem. Soc.* **2003**, *150*, A1457.
- [6] B. B. Kopuklu, E. Esen, A. Gomez-Martin, M. Winter, T. Placke, R. Schmuck, S. A. Gursel, A. Yurum, *ACS Appl. Mater. Interfaces* **2022**, *14*, 34665.
- [7] M. Wetjen, D. Pritzl, R. Jung, S. Solchenbach, R. Ghadimi, H. A. Gasteiger, *J. Electrochem. Soc.* **2017**, *164*, A2840.
- [8] V. Müller, R. G. Scurtu, K. Richter, T. Waldmann, M. Memm, M. A. Danzer, M. Wohlfahrt-Mehrens, *J. Electrochem. Soc.* **2019**, *166*, A3796.
- [9] M. W. Forney, M. J. Ganter, J. W. Staub, R. D. Ridgley, B. J. Landi, *Nano Lett.* **2013**, *13*, 4158.
- [10] J. S. Kim, W. Pfleging, R. Kohler, H. J. Seifert, T. Y. Kim, D. Byun, H. G. Jung, W. Choi, J. K. Lee, *J. Power Sources* **2015**, *279*, 13.
- [11] J. Guo, A. Sun, X. Chen, C. Wang, A. Manivannan, *Electrochim. Acta* **2011**, *56*, 3981.
- [12] J. Bareño, I. A. Shkrob, J. A. Gilbert, M. Klett, D. P. Abraham, *J. Phys. Chem. C* **2017**, *121*, 20640.
- [13] G. Li, J. Y. Yue, Q. Xu, T. T. Zuo, Y. X. Yin, Y. G. Guo, *Nano Energy* **2019**, *60*, 485.
- [14] M. Arnaiz, D. Shanmukaraj, D. Carriazo, D. Bhattacharjya, A. Villaverde, M. Armand, J. Ajuria, *Energy Environ. Sci.* **2020**, *13*, 2441.
- [15] P. Jeżowski, O. Crosnier, E. Deunf, P. Poizot, F. Béguin, T. Brousse, *Nat. Mater.* **2018**, *17*, 167.
- [16] F. Jiang, Y. Sun, K. Zhang, Y. Liu, X. Feng, H. Xiang, *Electrochim. Acta* **2021**, *398*, 139315.
- [17] C. R. Jarvis, M. J. Lain, M. V. Yakovleva, Y. Gao, *J. Power Sources* **2006**, *162*, 800.
- [18] H. Zhao, Z. Wang, P. Lu, M. Jiang, F. Shi, X. Song, Z. Zheng, X. Zhou, Y. Fu, G. Abdelbast, X. Xiao, *Nano Lett.* **2014**, *14*, 6704.
- [19] N. Liu, L. Hu, M. T. McDowell, A. Jackson, Y. Cui, *ACS Nano* **2011**, *5*, 6487.
- [20] H. Sun, X. He, J. Ren, J. Li, C. Jiang, C. Wan, *Electrochim. Acta* **2007**, *52*, 4312.
- [21] D. Shanmukaraj, S. Grugeon, S. Laruelle, G. Douglade, J. M. Tarascon, M. Armand, *Electrochim. Commun.* **2010**, *12*, 1344.
- [22] P. Bärmann, M. Mohrhardt, J. E. Frerichs, M. Helling, A. Kolesnikov, S. Klabunde, S. Nowak, M. R. Hansen, M. Winter, T. Placke, *Adv. Energy Mater.* **2021**, *11*, 2100925.
- [23] E. Esen, M. Mohrhardt, I. Lennartz, I. de Meatza, M. Schmuck, M. Winter, E. Paillard, *Mater. Today Chem.* **2023**, *30*, 101587.
- [24] J. Wellmann, J. P. Brinkmann, B. Wankmüller, K. Neuhaus, U. Rodehorst, M. R. Hansen, M. Winter, E. Paillard, *ACS Appl. Mater. Interfaces* **2021**, *13*, 34227.
- [25] M. S. Ding, S. L. Koch, S. Passerini, *Electrochim. Acta* **2017**, *240*, 408.
- [26] S. P. Kühn, F. Pfeiffer, M. Bela, U. Rodehorst, D. Weintz, M. Stan, M. Baghernejad, M. Winter, I. Cekic-Laskovic, *J. Power Sources* **2022**, *549*, 232118.
- [27] J. Zhao, Z. Lu, N. Liu, H.-W. Lee, M. T. McDowell, Y. Cui, *Nat. Commun.* **2014**, *5*, 5088.
- [28] C. A. Augustine, D. Panoth, A. Paravanno, *ChemistrySelect* **2019**, *4*, 7090.
- [29] X. Wang, C. Liu, S. Zhang, H. Wang, R. Wang, Y. Li, J. Sun, *ACS Appl. Energy Mater.* **2021**, *4*, 5246.
- [30] X. Chen, G. Ge, W. Wang, B. Zhang, J. Jiang, X. Yang, Y. Li, L. Wang, X. He, Y. Sun, *Sci. China Chem.* **2021**, *64*, 1417.
- [31] J. Lu, Y. Wang, Y. Qiao, S. Yang, X. Cheng, M. Yang, J. Zhang, Z. Fu, *Energy Storage Mater.* **2024**, *66*, 103204.
- [32] A. R. Jiménez, R. Nölle, R. Wagner, J. Hüsker, M. Kolek, R. Schmuck, M. Winter, T. Placke, *Nanoscale* **2018**, *10*, 2128.
- [33] W. Choi, H. C. Shin, J. M. Kim, J. Y. Choi, W. S. Yoon, *J. Electrochem. Sci. Technol.* **2020**, *11*, 1.
- [34] F. Holtstiege, P. Bärmann, R. Nölle, M. Winter, T. Placke, *Batteries (Basel)* **2018**, *4*, 4.
- [35] M. A. Danzer, *Batteries (Basel)* **2019**, *5*, 53.
- [36] A. Tokranov, R. Kumar, C. Li, S. Minne, X. Xiao, B. W. Sheldon, *Adv. Energy Mater.* **2016**, *6*, 1502302.
- [37] M. Gaberscek, J. Moskon, B. Erjavec, R. Dominko, J. Jamnik, *Electrochim. Solid-State Lett.* **2008**, *11*, A170.
- [38] D. Pritzl, A. E. Bumberger, M. Wetjen, J. Landesfeind, S. Solchenbach, H. A. Gasteiger, *J. Electrochem. Soc.* **2019**, *166*, A582.
- [39] M. Holzapfel, A. Martinent, F. Alloin, B. L. Gorrec, R. Yazami, C. Montella, *J. Electroanal. Chem.* **2003**, *546*, 41.
- [40] S. A. Delp, O. Borodin, M. Olguin, C. G. Eisner, J. L. Allen, T. R. Jow, *Electrochim. Acta* **2016**, *209*, 498.
- [41] S. Laruelle, S. Pilard, P. Guenot, S. Grugeon, J. M. Tarascon, *J. Electrochem. Soc.* **2004**, *151*, A1202.
- [42] K. Nishikawa, J. Moon, K. Kanamura, *J. Power Sources* **2016**, *302*, 46.
- [43] H. Wang, W. Wu, Q. Jia, T. Liu, F. Liu, M. Zhang, M. Bai, S. Li, X. Tang, B. Gan, Y. Ma, *Ind. Eng. Chem. Res.* **2022**, *61*, 7442.
- [44] M. S. Milien, U. Tottempudi, M. Son, M. Ue, B. L. Lucht, *J. Electrochem. Soc.* **2016**, *163*, A1369.
- [45] K. S. Siow, L. Britcher, S. Kumar, H. J. Griesser, *Plasma Processes Polym.* **2014**, *11*, 133.
- [46] X. Ren, L. Zou, X. Cao, M. H. Engelhard, W. Liu, S. D. Burton, H. Lee, C. Niu, B. E. Matthews, Z. Zhu, C. Wang, *Joule* **2019**, *3*, 1662.
- [47] A. L. Michan, M. Leskes, C. P. Grey, *Chem. Mater.* **2016**, *28*, 385.
- [48] Y. Jin, N. Kneusel, L. E. Marbella, E. Castillo-Martínez, P. C. Magusin, R. S. Weatherup, E. Jónsson, T. Liu, S. Paul, C. P. Grey, *J. Am. Chem. Soc.* **2018**, *140*, 9854.
- [49] P. Niehoff, M. Winter, *Langmuir* **2013**, *29*, 15813.
- [50] K. Xu, U. Lee, S. Zhang, M. Wood, T. R. Jow, *Electrochim. Solid-State Lett.* **2003**, *6*, A144.
- [51] B. S. Parimalam, B. L. Lucht, *J. Electrochem. Soc.* **2018**, *165*, A251.
- [52] M. Nie, D. P. Abraham, Y. Chen, A. Bose, B. L. Lucht, *J. Phys. Chem. C* **2013**, *117*, 13403.
- [53] Y. Okuno, K. Ushirogata, K. Sodeyama, Y. Tateyama, *Phys. Chem. Chem. Phys.* **2016**, *18*, 8643.
- [54] H. Wang, H. B. Chew, *ACS Appl. Mater. Interfaces* **2017**, *9*, 25662.
- [55] Q. Li, X. Liu, X. Han, Y. Xiang, G. Zhong, J. Wang, B. Zheng, J. Zhou, Y. Yang, *ACS Appl. Mater. Interfaces* **2019**, *11*, 14066.
- [56] M. Swietoslawski, M. Molenda, E. Esen, R. Dziembaj, *ECS Trans.* **2014**, *62*, 89.
- [57] N. Qin, J. Chen, Y. Lu, Y. Li, W. Cai, J. Li, C. Zhang, Z. Chen, J. P. Zheng, L. Jin, *ACS Energy Lett.* **2024**, *9*, 4843.

- [58] L. Benitez, J. M. Seminario, *J. Phys. Chem. C* **2016**, *120*, 17978.
- [59] B. Han, Z. Zhang, Y. Zou, K. Xu, G. Xu, H. Wang, H. Meng, Y. Deng, J. Li, M. Gu, *Adv. Mater.* **2021**, *33*, 2100404.
- [60] A. Zhou, J. Xu, X. Dai, B. Yang, Y. Lu, L. Wang, C. Fan, J. Li, *J. Power Sources* **2016**, *322*, 10.
- [61] C. Jayawardana, N. Rodrigo, B. Parimalam, B. L. Lucht, *ACS Energy Lett.* **2021**, *6*, 3788.
- [62] S. K. Heiskanen, N. Laszczynski, B. L. Lucht, *J. Electrochem. Soc.* **2020**, *167*, 100519.
- [63] S. M. Yun, J. W. Kim, M. J. Jung, Y. C. Nho, P. H. Kang, Y. S. Lee, *Carbon Lett.* **2007**, *8*, 292.
- [64] G. Cherkashinin, K. Nikolowski, H. Ehrenberg, S. Jacke, L. Dimesso, W. Jaegermann, *Phys. Chem. Chem. Phys.* **2012**, *14*, 12321.
- [65] A. Yulaev, V. Oleshko, P. Haney, J. Liu, Y. Qi, A. A. Talin, M. S. Leite, A. Kolmakov, *Nano Lett.* **2018**, *18*, 1644.
- [66] X. Zhu, Z. Lin, J. Lai, T. Lv, T. Lin, H. Pan, J. Feng, Q. Wang, S. Han, R. Chen, L. Chen, L. Suo, *Angew. Chem., Int. Ed.* **2024**, *63*, e202317549.
- [67] R. Dedryvère, L. Gireaud, S. Grueon, S. Laruelle, J. M. Tarascon, D. Gonbeau, *J. Phys. Chem. B* **2005**, *109*, 15868.
- [68] Y. Gao, T. Rojas, K. Wang, S. Liu, D. Wang, T. Chen, H. Wang, A. T. Ngo, D. Wang, *Nat. Energy* **2020**, *5*, 534.
- [69] S. Shiraishi, K. Kanamura, Z. Takehara, *J. Appl. Electrochem.* **1995**, *25*, 584.
- [70] M. Herstedt, D. P. Abraham, J. B. Kerr, K. Edström, *Electrochim. Acta* **2004**, *49*, 5097.
- [71] P. Niehoff, S. Passerini, M. Winter, *Langmuir* **2013**, *29*, 5806.
- [72] Y. Kwan, G. M. Ng, C. Huan, *Thin Solid Films* **2015**, *590*, 40.
- [73] M. Schulze, M. Lorenz, N. Wagner, E. Gültzow, *Fresenius' J. Anal. Chem.* **1999**, *365*, 106.
- [74] M. C. Hsiao, S. H. Liao, M. Y. Yen, P. I. Liu, N. W. Pu, C. A. Wang, C. C. M. Ma, *ACS Appl. Mater. Interfaces* **2010**, *2*, 3092.

Manuscript received: July 6, 2025

Revised manuscript received: September 27, 2025

manuscriptRevised October 17, 2025

Version of record online: